KLA INSTRUMENTS

Effect of Ultraviolet C Disinfection on Physical Properties of N95 Face Masks

Nano Indenter® G200X and Zeta-20 Optical Profiler

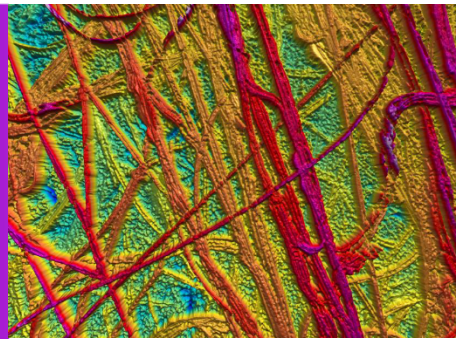

Introduction

The unprecedented COVID-19 pandemic has led to critical shortages of personal protective equipment (PPE). N95 masks are one of the key PPEs to protect frontline healthcare workers, and these devices are intended to be used once and then disposed. The N95 filtering facepiece respirator (FFR) face mask is typically composed of multiple filtration layers, including those shown in Figure 1, with the inner filtration layer considered to be the key functional component[1]. This layer is made from melt blown non-woven fabric, which is composed of thousands of very thin, noncontinuous fibrils. An electric charge on the fibers enables a 10x higher filtration efficiency and low pressure drop, due to a technique called corona electrostatic charging applied to the N95 filtration layer during manufacturing[2]. Polypropylene (PP) is the most widely-used raw material for the melt blown fibrils due to its low melting point. Figure 2 shows the SEM picture of the primary filtration layers.

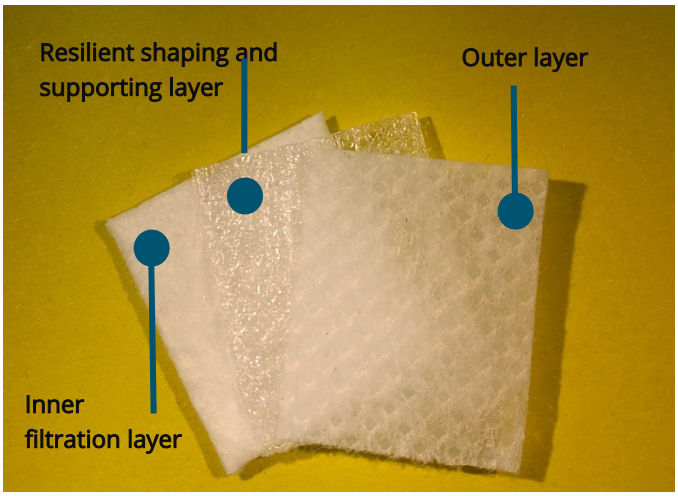

Figure 1. An N95 respirator coupon sample shows the three layers of nonwoven material: the inner filtration layer is melt blown (non-woven) polypropylene to provide effective filtration; the middle layer provides the mask shape and supports the inner and outer layers; and the outer layer provides filtration for larger particles. The FFR model selected for this research was the 3M 9211+ N95 respirator, with the inner filtration layer selected for testing.

Due to the limited supply of N95 FFRs, The Centers for Disease Control (CDC) made recommendations on risk management approaches for the use of these masks and provided guidance regarding limited or extended reuse of N95 FFRs by healthcare workers. Based on the limited research available, three methods have shown the most promise in decontaminating N95 FFRs for reuse: (1) ultraviolet germicidal irradiation (UVGI), (2) vaporous hydrogen peroxide, and (3) moist heat[3]. Previous research demonstrated that the UVGI technique, which used a wavelength range of light that fell in the ultraviolet C spectrum (short-wavelength ultraviolet, where λ = 100-280nm), could inactivate influenza and coronaviruses in N95 FFRs by penetrating the mask and damaging the molecular bonds that hold together the nucleic acids of viruses and bacteria to prevent them from infecting and/or replicating in human cells[4]. The genomic materials DNA and RNA have a maximum absorption wavelength of around 260nm[5,6]. As of October 2020, the UVC inactivation of the COVID-19 virus in N95 FFRs has not been demonstrated in peer-reviewed studies. However, UVGI decontamination has been widely applied in hospitals to inactivate airborne pathogens. Its efficiency is critically dependent on both UV wavelength (nm) and UVC dose (J/cm^2). When the UVC light passes through the multiple mask layers, the structure of the N95 FFR causes a drop in transmitted light intensity. Therefore, for effective decontamination, the required UVC dose at the N95 respirator surface is several hundred-fold greater than the dose needed for virus inactivation on surfaces or in the air. The currently suggested procedure for UVC treatment considers a minimum of 1J/cm^2 as the marginally acceptable UVC dose for N95 FFR decontamination[7].

There is risk of damage to the N95 respirator materials after multiple decontamination cycles, and one reason is that UV radiation degrades polymers. Lindsley et al. studied the effects of four different UVGI treatments on N95 respirator filtration performance and structural integrity, with a specific interest in how large a cumulative UVGI dose that respirators can withstand[8]. Bursting strength tests on N95 structures

composed of tangled and spun-bonded polypropylene fibers demonstrated that UVC treatment dramatically decreased the strength of N95 layers. There are also concerns about electrical charge loss by the filtration fibers during UVC treatment[9]. Considering these factors, it is important to understand the UVC effect on the nanoscale physical properties of the individual fibers.

Experimental Method

A 3M 9211+ N95 respirator mask was cut into 1cm square coupons and placed into a Thermo Scientific Prisma scanning electron microscope (SEM). The SEM was operated a low voltage of 1.00kV and the respirator structure was studied using an Everhart-Thornley SE detector. The resulting SEM images are shown in Figures 2-4. Six additional coupons of the melt blown layer were cut from the same respirator and placed in a cardboard chamber and exposed to UVC light with a primary wavelength of 254nm. The chamber was equipped with two 38W parallel lamps, and the fiber samples were positioned 30cm from the lamps when exposed to the UVC light. Samples were left in the chamber for 5, 35, 65, 95 and 155 minutes, resulting in cumulative exposures of 1, 7, 13, 19 and 31J/cm^2 of UVC, for a total of five test conditions, plus an untreated sample. The chamber temperature was monitored, with a mean temperature during exposure of 24.5°C. The nanoindentation measurements were conducted at 22°C and data were randomly collected on different fibers and fiber positions . A minimum of 10 test was performed under each condition for statistical analysis. The UVC dose was defined as:

$$\text{UVC dose} \propto \frac{\text{UV bulb power} * \text{Exposure time}}{4 * \pi * \text{UV bulb distance}^2} \qquad (1)$$

where the UV bulb distance is the 30cm between the lamps and the sample puck position. For nanoindentation measurement, the N95 respirator melt blown layer microfibers were prepared under the following protocol:

1. The N95 respirator microfibers were untangled and placed on painter's tape, pushed down firmly to make good adhesive contact with the tape.
2. A thin layer of epoxy was applied to the aluminum sample stub.
3. The microfibers were placed on the epoxy and pushed firmly to make solid contact with the aluminum stub.
4. The tape was removed after the epoxy cured.

The undersides of the microfibers were surrounded by epoxy resin, and the epoxy-free portions of the fibers were scanned using the KLA Nano Indenter® G200X NanoVision option, which features a closed loop nano-positioning stage for high

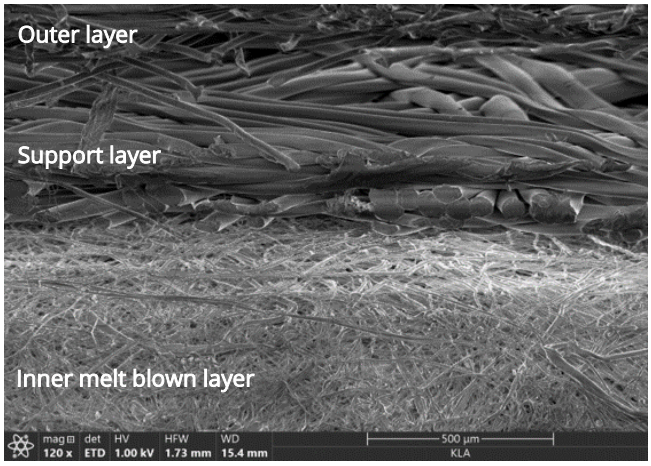

Figure 2. Scanning electron microscopy (SEM) image of the cross section of commercial N95 mask material, showing the electrocharged layers.

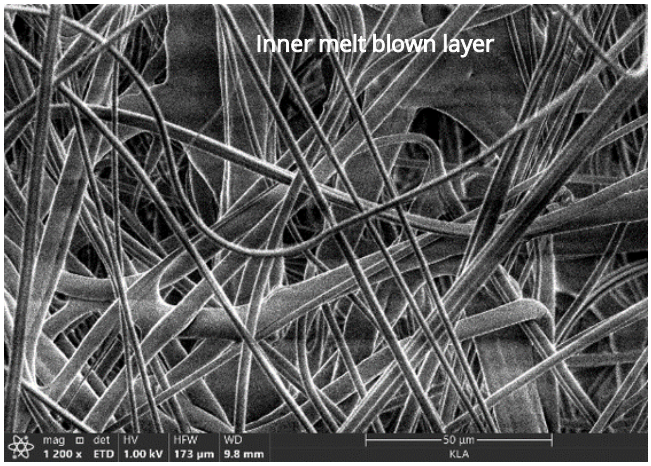

Figure 3. SEM image of the inner filtration layer reveals the melt blown fibers forming the porous network structure.

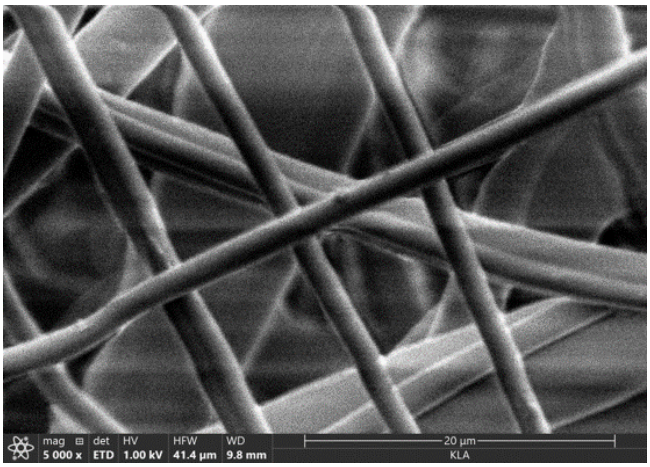

Figure 4. SEM image showing the individual melt blown fibers.

resolution 3D imaging and precise targeting to characterize individual phases of complex materials. NanoVision enables researchers to examine residual impressions in order to quantify material response phenomena such as pile-up, deformation volume and fracture toughness. The nanoindentation testing was conducted using the CSM option and an InForce 50 actuator fitted with a Berkovich indenter. With the CSM option, Young's modulus and hardness are measured as a continuous function of penetration[10]. Results were generated using the InView test method **Advanced Dynamic E and H**, which allows the measurement of Young's modulus and hardness of small volume materials, such as PP fibers.

The topography and width measurements of the fiber clusters were obtained by imaging the coupons with a KLA Zeta-20 optical profiler. The Zeta-20 microscope utilizes proprietary ZDot™ technology to provide non-contact 3D topographic measurement, enabling the user to quickly explore large sample areas to locate smaller regions of interest for further analysis. As compared to a scanning electron microscope, the Zeta optical profiler provides True Color 3D imaging, is fast and easy to operate, requires minimal sample preparation, and avoids sample outgassing, damage and/or contamination due to the SEM measurement itself. This non-contact, non-damaging method allows additional metrology techniques such as FTIR and Raman spectroscopy to be applied to the exact same sample to provide further analysis data without concern that the previous metrology may have altered the sample either physically or chemically. For this study, the ZDot structured illumination imaging mode was used to produce 3D True Color images for measuring the PP fiber width. The fiber width sampling at each dose was based on five different sites measuring five fibers per site, for a total of 25 width measurements per dose.

Results and Discussion

Figure 2 shows the scanning electron microscopy (SEM) image for the layer cross section, taken from the 3M 9211+ N95 respirator. The inner filtration layer was made up of non-woven polypropylene fibers that were tangled to form a three-dimensional porous structure. Figures 3 and 4 show the inner melt blown filtration layer microstructure at higher magnification. The average fiber diameter was about 1-2µm.

Figure 5 shows two 16µm x 16µm NanoVision scans of the N95 respirator melt blown microfiber. Figure 5 (top) shows the surface of the microfiber and epoxy prior to nanoindentation and Figure 5 (bottom) shows the same region after three

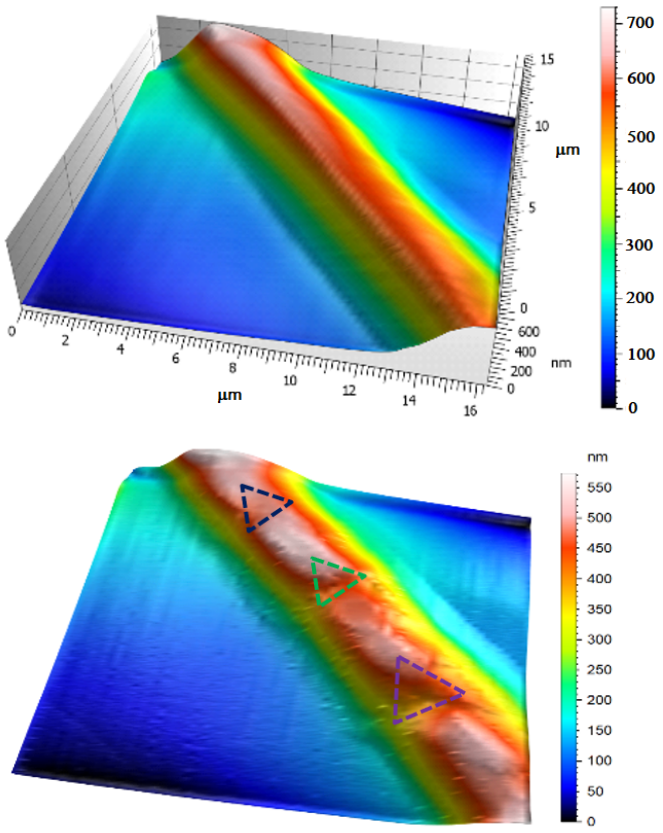

Figure 5. N95 respirator filtration fiber testing using the KLA Nano Indenter G200X with NanoVision scanning, showing an individual fiber before (top) and after (bottom) nanoindentation, where the bottom image shows the three residual marks on the fiber. 16µm x 16µm scan of single melt blown non-woven fiber over 0.6µm height. Images shown after three point leveling.

nanoindentation tests were performed on the fiber under maximum loads of 0.1mN, 0.3mN and 0.5mN. Both figures clearly represent the very high resolution and accuracy of indent placement capability of the NanoVision option.

The load-displacement curves for the three tests are shown in Figure 6, with the line color for each curve corresponding to the mark indicators from Figure 5. Indentation elastic recovery was observed on the unloading segments, generating different residual displacements. Using the 3D scanning probe microscopy (SPM) image, the residual indentation size and depth were also measured, based on the surface profile along the longitudinal axis of the fiber. Residual depth measurements are shown in Figure 7, where the loads of 0.1mN, 0.3mN and 0.5mN resulted in residual indentation depths of 57nm, 107nm and 147nm, respectively, which is consistent with the indentation load and depth curves. The inset image in Figure 7 shows the profile location on the fiber.

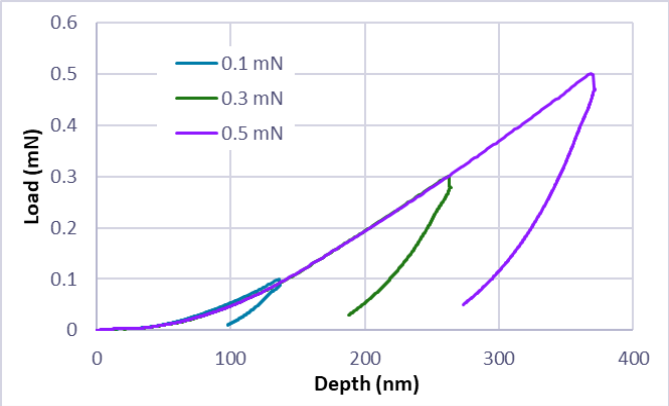

Figure 6. Load-displacement curves corresponding to the three indentation tests are shown. Line color corresponds to indentation mark color from Figure 5.

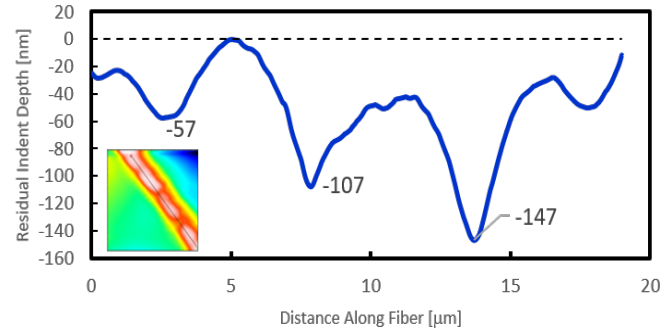

Figure 7. A surface profile across the indentation marks measured the depth of each of the three residual indentations, with the profile location on the fiber also shown (inset).

For the indentation measurements, loading was terminated at a penetration depth ≥ 500nm. The Young's modulus and hardness were investigated on PP fibers that were exposed to different cumulative doses of UVC light. Young's modulus (E) is a measure of material stiffness, and is defined as:

$$E = \frac{\sigma}{\varepsilon} \qquad (2)$$

where σ is the uniaxial stress and ε is the resulting strain, or proportional deformation of the material. Hardness (H) is a function of the maximum applied load and the resulting plastic deformation of the material, and is defined as:

$$H = \frac{P_{max}}{A} \qquad (3)$$

where P_{max} is the maximum applied load and A is the area of the plastic deformation. The process of extracting E and H from Equations (2) and (3) assumes that a Berkovich indenter drives into a semi-infinite solid. However, indentation measurement in this case was performed on the curved surface of the PP fibers. It is possible that the Oliver-Pharr method results in underestimation of hardness because of the effects of free surface. Nevertheless, we adopted the same method for comparative purposes. The absolute values of the PP fiber nanomechanical properties will be impacted by the free surfaces, but the relative changes are the same.

Figure 8 shows nanoindentation load and displacement curves of PP fibers for each of the five UVC doses. A noticeable difference between the indentation responses of the five samples is the displacement during the loading and holding segments. In general, when the UVC exposure dose was high, the curves shifted slightly to the right while the maximum load decreased significantly at the same indentation depth. The physical changes to the fibers at higher doses are reflected in the hardness and Young's modulus results.

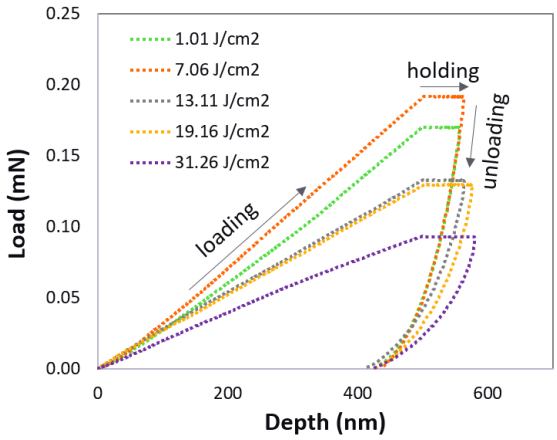

Figure 8. Nanoindentation load and displacement curves of PP fibers subjected to five different doses of UVC light. The maximum load decreases at higher doses. The arrows indicate the depth response versus load in the order in which the loading was applied.

Figure 9 represents the indentation hardness (top) and Young's modulus (bottom), as a continuous function of depth for the five doses. Figure 10 shows the PP fiber hardness (top) and Young's modulus (bottom) at an indentation depth of 500nm, where the quantities have largely stabilized, for the five different UVC doses. When the UVC dosage was raised from 0 to 1J/cm2, a precipitous drop in hardness and a significant drop in modulus were observed. Further increase of UVC dosage to 7J/cm2 appears to result in a small increase of fiber hardness and possibly a small increase in modulus as well. At higher UVC doses, both hardness and modulus decrease monotonically with increased UVC dose. Overall, the observed relationship between UVC dose and reduction in hardness and modulus of the N95 fibers is consistent with previous research on the UVC

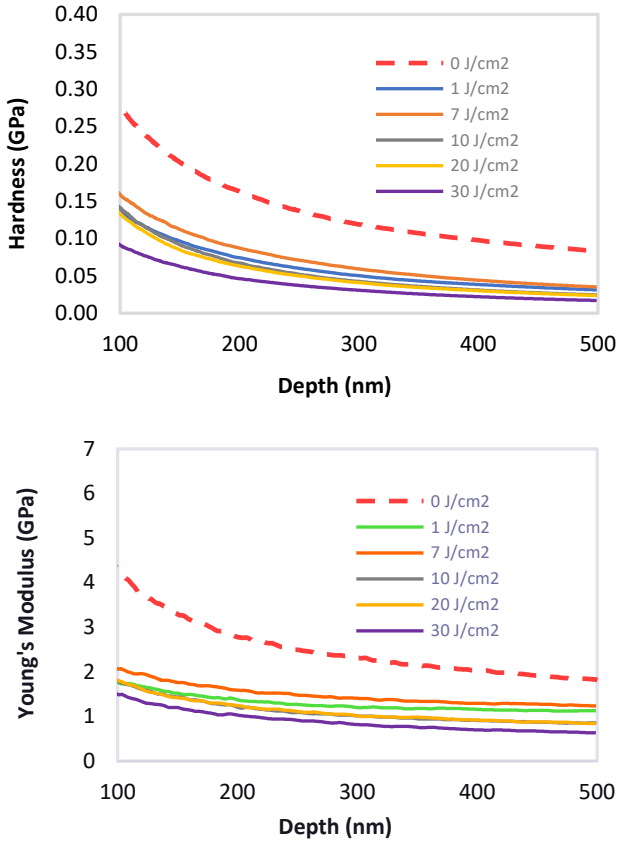

Figure 9. Nanoindentation hardness (top) and Young's modulus (bottom) of PP fibers subjected to five different doses of UVC light.

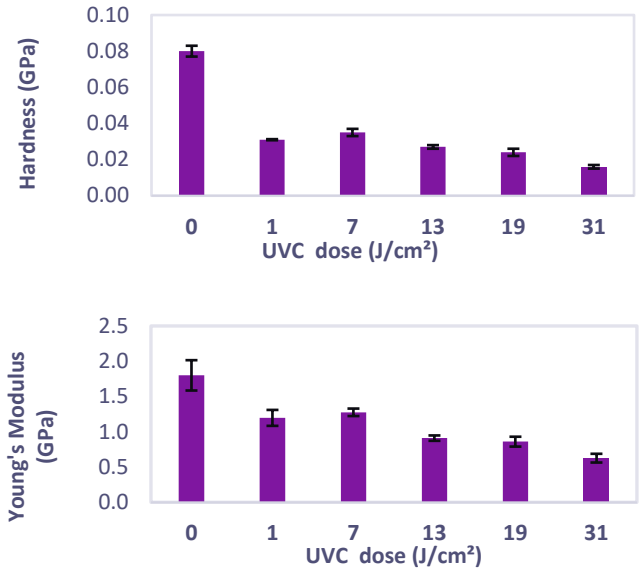

Figure 10. The hardness (top) and Young's modulus (bottom) of PP fibers exposed at different UVC doses. Data are reported for an indentation depth of 500nm.

sensitivity of polypropylene fibers[11]. Polypropylene has been reported to be especially susceptible to UV damage. It experiences photooxidative degradation in the presence of UV light due to breakage of the main molecular chains of the PP, causing brittleness and loss of tensile, impact and elongation strengths. Whether the lower dose regime of 1J/cm^2 to 7J/cm^2 represents a deviation from the overall monotonic relationship between dose and hardness/modulus would require further study.

Figure 11 shows a 3D Zeta image of the N95 respirator melt blown layer with no UVC treatment. The untreated fibers appear to be tangled and variable in size and shape, with some fibers joining to form large bundles. This True Color image appears to be largely grayscale due to the translucence of the fibers and the dark background of the sample mounting surface.

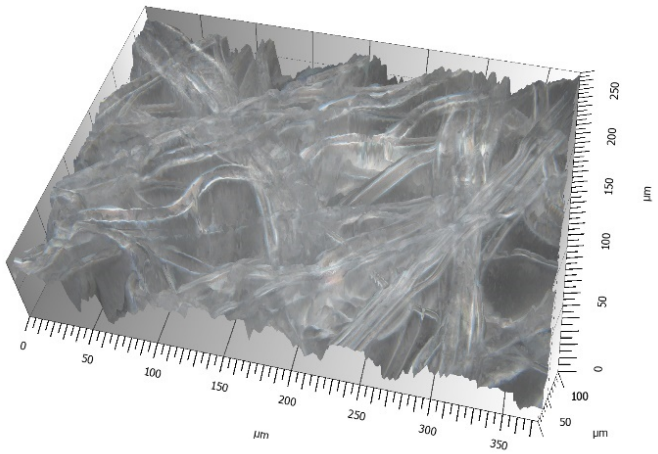

Figure 11. True Color image of the untreated N95 respirator melt blown layer. Gray level variation is due to translucence of the sample fibers and the dark sample mounting surface.

Figure 12 shows the N95 respirator melt blown layer topography following different UVC treatment conditions, with height variation represented by color. With no UVC exposure, the fibers appear larger in width and more bundled. Voids between the fibers appear smaller as compared to the UVC-treated samples. Following UVC treatment, the fiber width shrinks after an initial dose of 1J/m^2. At higher doses, the fibers also appear to separate from each other.

Fiber width analysis was derived from the 3D images by selecting 25 random fibers and measuring the widths. Average fiber width as a function of UVC dose is shown in Figure 13. The data shows that the average fiber width decreases 37% at 1J/cm^2 of UVC dose and continues to decrease until a dose of

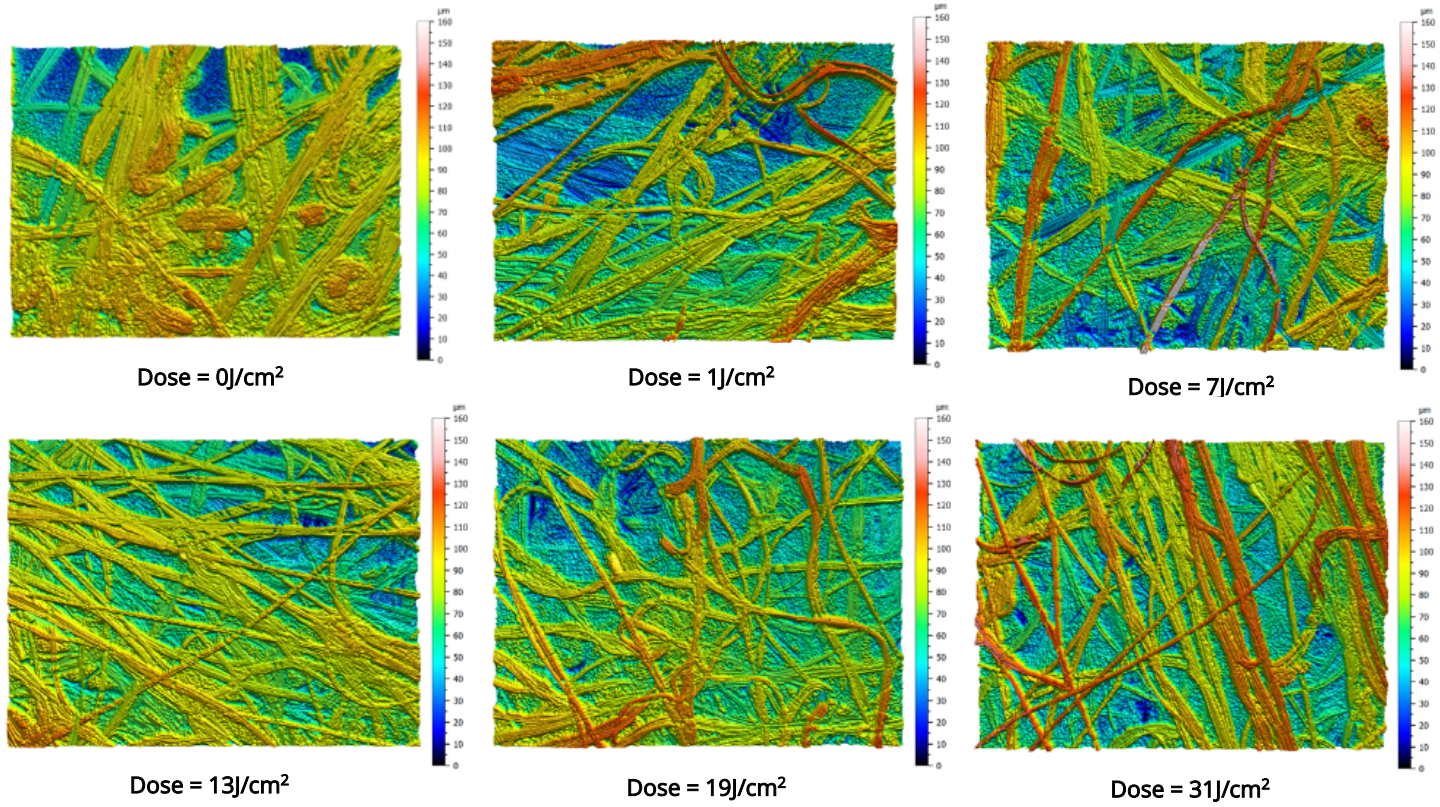

Figure 12. Zeta-20 images of the melt blown layer of the N95 respirator with different UVC doses: (a) 0J/cm²; (b) 1J/cm²; (c) 7J/cm²; (d) 13J/cm²; (e) 19J/cm²; and (f) 31J/cm². Z scale is 0–160µm for all images.

19J/cm². During the 0 - 19J/cm² dosage range, the width data exhibits a strong and well-behaved logarithmic decrease with dosage, with R^2 = 0.95 (note that for the 0 - 13Jc/m² dosage range, R^2 = 0.99). At a dose of 31 J/cm², the trend saturated and no additional decrease was observed. Fiber width variability was also large for each 25-measurement average, and this variation could be attributed to the waviness and nonuniformity of the melt blown PP fibers.

Conclusions

In this work, the effect of UVC disinfection treatment on the nanomechanical and topographic properties of N95 respirator filtration fibers was investigated using a KLA Nano Indenter G200X with CSM and survey scanning options, as well as a Zeta-20 optical profiler. The NanoVision scanning image coupled with indent placement capability allowed measurements on individual fibers. An initial UVC dosage of 1J/cm² was shown to significantly decrease both Young's modulus (E), hardness (H). At higher UVC doses, the average E and H both continued to decrease, as measured on individual fibers. These results show that the PP microfiber layer loses its strength when N95 respirators are overexposed to accumulated doses of UVC

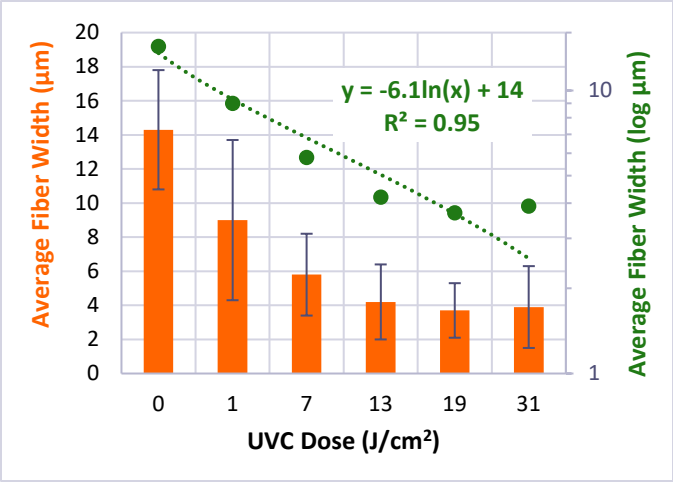

Figure 13. The average fiber width as a function of UVC dose appears to decrease logarithmically with increased dose, up to 19J/cm². Between 19 and 31J/cm², the width decrease appears to saturate, so the 31J/cm² data point was not included in the fit.

radiation during the process of decontamination. Loss of fiber strength can lead to small tears or holes in the mask, resulting in lowered protection against COVID-19 exposure. Furthermore, the fiber width also exhibits a logarithmic

decrease during UVC exposure, potentially providing openings for the virus to penetrate the mask.

Future work may include investigation of additional process conditions over time. In that case, the Zeta-20 could be used as a primary non-contact tool for characterizing and quantifying the transformation kinetics of fiber-texture agglomeration. This information may help guide comparisons and further improve the stability of N95 mask material constituents and processes.

For full details of this study, refer to "Effect of Ultraviolet C Disinfection Treatment on the Nanomechanical and Topographic Properties of N95 Respirator Filtration Microfibers," published in MRS Advances, September 2020.

Acknowledgement

KLA Instruments acknowledges the contributions of Dr. Peter Tsai, the inventor of the N95 respirator filter.

References

1. "Respirator Trusted-Source: Selection FAQs", U.S. National Institute for Occupational Safety and Health, 2020-03-12.
2. P.P. Tsai and L.C. Wadsworth, "Method and apparatus for the electrostatic charging of a web or film," US5401446A, United States Patent and Trademark Office,1992.
3. "Decontamination and Reuse of Filtering Facepiece Respirators," CDC (2020c, April 9), https://www.cdc.gov/coronavirus/2019-ncov/hcp/ppe-strategy/decontamination-reuse-respirators.html.
4. https://www.unionleader.com/news/health/coronavirus/unh-researchers-working-on-uv-disinfection-of-n95-masks/article_4192d764-2773-514d-b5c6-027be3379842.html.
5. J.G. Anderson, N.J. Rowan, S.J. MacGregor, R.A. Fouracre and O. Farish, "Inactivation of food-borne enteropathogenic bacteria and spoilage fungi using pulsed-light," IEEE Transactions on Plasma Science, IEEE Nuclear and Plasma Sciences Society , volume 28 (1) (2000), 83–88, https://doi.org/10.1109/27.842870.
6. A. Ito and T. Ito, "Absorption spectra of deoxyribose, ribosephosphate, ATP and DNA by direct transmission measurements in the vacuum-UV (150-190 nm) and far-UV (190-260 nm) regions using synchrotron radiation as a light source," Photochemistry and Photobiology , volume 44 (3), (1986) 355–358, https://doi.org/10.1111/j.1751-1097.1986.tb04675.x.
7. J.J. Lowe, K.D. Paladino, J.D. Farke, K. Boulter, K. Cawcutt, M. Schwedhelo, A. Vasa, M. Wadman, S. Watson and M.E. Rupp, M.E, "N95 Filtering Facepiece Respirator Ultraviolet and Reuse," Nebraska Medicine (2020), https://www.nebraskamed.com/sites/default/files/documents/covid-19/n-95-decon-process.pdf.
8. W.G. Lindsley, S.B. Martin, R.E. Thewlis, K. Sarkisian, J.O. Nwoko, K.R. Mead and J.D. Noti, J. D., "Effects of Ultraviolet Germicidal Irradiation (UVGI) on N95 Respirator Filtration Performance and Structural Integrity," Journal of Occupational and Environmental Hygiene , volume 12 (8), (2015) 509–517, https://doi.org/10.1080/15459624.2015.1018518.
9. P.P. Tsai, "Performance of Masks and Discussion of the Inactivation of SARS-CoV-2," Engineered Science, 10.30919/es8d1110 (2020).
10. J.L. Hay, P. Agee and E.G. Herbert, "Continuous stiffness measurement during instrumented indentation testing," Experimental Techniques, volume 34 (3), (2010) 86-94.
11. B.N. Keene, "Biodegradation of Polypropylene Nonwovens," Ph.D. Thesis, North Carolina State University, AAT 3538393, ISBN: 9781303012310 (2012).

KLA Corporation
One Technology Drive
Milpitas, CA 95035
Printed in the USA
Rev 9 2021-03-04